

Lightning Interferometric Processing and Uncertainty Analysis for General Noncoplanar Antenna Arrays

Xuan-Min Shao¹, Cheng Ho¹, Collin S. Meierbachtol¹, and Dale Anderson¹

¹Los Alamos National Laboratory (DOE)

November 24, 2022

Abstract

Broadband radio frequency interferometric technique is being rapidly advanced in recent years and is being increasingly widely used in the lightning community for detailed discharge physics studies. Los Alamos National Laboratory is in the process of deploying two spatially separated interferometers that consist of four, dual-polarization antennas for each interferometer. For a 4-antenna array, or any array that consists of more than three antennas, the antennas cannot be assumed situated in the same plane, and a generic interferometric process is needed to take the full advantage of the additional antennas. In this paper we present and numerically verify an analytic solution for a general noncoplanar array that directly relates the source direction to the array geometry and the time delay measurement. This general and analytic solution can be used in any array configurations with three or more antennas. We then derive the analytic formulas for the associated interferometric uncertainties based on the general analytic solution. Uncertainty analysis is critically important for correct and credible interpretation of the observations, but only very limited and incomplete uncertainty analyses have been reported in the lightning community. In this paper, we first carry out the uncertainty analysis for a pair of baselines and then extend the analysis to a combination of multiple pairs of baselines. We verify the analytic uncertainty analyses with numerical experiments and discuss the behavior of the uncertainties. These analyses will hopefully help to lay the foundation for future uncertainty estimate, and for more statistically trustworthy interpretation of the interferometric observations.

Hosted file

essoar.10507768.1.docx available at <https://authorea.com/users/532719/articles/603672-lightning-interferometric-processing-and-uncertainty-analysis-for-general-noncoplanar-antenna-arrays>

Lightning Interferometric Processing and Uncertainty Analysis for General Noncoplanar Antenna Arrays

Xuan-Min Shao, Cheng Ho, Collin S. Meierbachtol, and Dale Anderson

Los Alamos National Laboratory

Corresponding author: Xuan-Min Shao

To be submitted to JGR-Atmosphere

LA-UR-21-28149

Main points:

1. A generic and analytic source direction solution is derived for general noncoplanar lightning interferometer arrays.
2. Analytic analyses of uncertainties are presented for a pair of baselines and for a combination of any number of pairs of baselines.
3. All analytic analyses are verified with numerical experiments and can be readily implemented in future interferometric observations.

Abstract

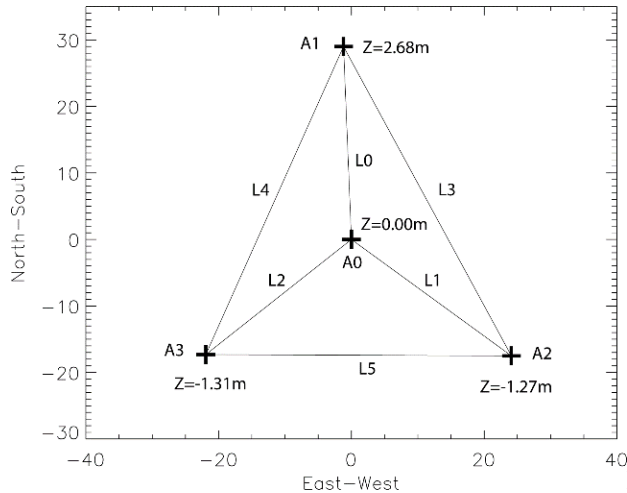
Broadband radio frequency interferometric technique is being rapidly advanced in recent years and is being increasingly widely used in the lightning community for detailed discharge physics studies. Los Alamos National Laboratory is in the process of deploying two spatially separated interferometers that consist of four, dual-polarization antennas for each interferometer. For a 4-antenna array, or any array that consists of more than three antennas, the antennas cannot be assumed situated in the same plane, and a generic interferometric process is needed to take the full advantage of the additional antennas. In this paper we present and numerically verify an analytic solution for a general noncoplanar array that directly relates the source direction to the array geometry and the time delay measurement. This general and analytic solution can be used in any array configurations with three or more antennas. We then derive the analytic formulas for the associated interferometric uncertainties based on the general analytic solution. Uncertainty analysis is critically important for correct and credible interpretation of the observations, but only very limited and incomplete uncertainty analyses have been reported in the lightning community. In this paper, we first carry out the uncertainty analysis for a pair of baselines and then extend the analysis to a combination of multiple pairs of baselines. We verify the analytic uncertainty analyses with numerical experiments and discuss the behavior of the uncertainties. These analyses will hopefully help to lay the foundation for future uncertainty estimate, and for more statistically trustworthy interpretation of the interferometric observations.

1. Introduction

Broadband radio frequency (RF) interferometry is playing an increasingly important role in lightning observations since its first introduction over two decades ago (Shao et al., 1996), and is now widely used in the lightning community for detailed physics understandings of lightning discharge processes (e.g., Belz et al., 2020; Dong et al., 2001; Huang et al., 2021; Jensen et al., 2021; Lyu et al., 2019; Rison et al., 2016; Shao et al., 2018, 2020; Stock et al., 2014, 2017; Sun et al., 2013; Tilles, et al., 2019). Many recent new understandings and discoveries of lightning physics, notably processes related to lightning initiation, can be attributed to broadband RF interferometric observations (e.g., Huang et al., 2021; Rison et al., 2016; Shao et al., 2020; Tilles, et al., 2019). As a result, broadband interferometry techniques have been advanced rapidly in recent years, with improved broadband data acquisition and processing techniques, and more recently with increased number of antennas for a more redundant and diversified baseline configuration.

Los Alamos National Laboratory (LANL) is in the process of deploying a two-station, four-antenna, polarized interferometer for 3-dimensional lightning RF source location and polarization measurement, in an expansion of its previous single-station, three-antenna broadband interferometric mapping and polarization (BIMAP) observations (Shao et al., 2018, 2020). As discussed in our earlier satellite observations (Shao and Jacobson, 2001, 2002) and in our more recent ground-based BIMAP studies, RF polarization detection provides a next-level insight into the physics of lightning discharge processes. However, a single-station BIMAP system only provides a 2-D source location and a 2-D polarization state that leaves possibilities for ambiguous physics interpretation of the observations. The goal of the new 3-D BIMAP observation (BIMAP-3D) is to eliminate these undesired ambiguities and to provide a more complete insight into the discharge physics.

However, before combining the 2-station BIMAP for 3-D observations, it is essential to improve the interferometric technique itself to take the full advantage of the new 4-antenna (instead of previous 3-antenna) arrays for the BIMAP-3D system and to understand the associated uncertainties with the single-station interferometric observations, and that are the focus of this study.



BIMAP-3D's four anten-

nas at each station form a roughly Y-shaped array (e.g., Figure 1). Such an array will provide six independent baselines instead of three baselines for a 3-antenna array and is expected to improve the interferometric performance. However, unlike a 3-antenna array, the four antennas cannot be assumed to be situated in the same (e.g., horizontal) plane, as in the case of Figure 1 where the four antennas are placed at different heights due to the local topography. For a 3-antenna array, if the plane of the array is not in parallel with the local horizontal plane, the sources can be first mapped referenced to the array's plane and then geometrically transformed to a coordinate frame that aligned with the local horizontal plane, as had been done in our earlier BIMAP observations. A similar approach can be applied to an array with four or more antennas, but that will limit to groups of three neighboring antennas that form closed triangles, and will not take the full advantage of other baseline combinations, for instance, the baseline pair of L0 and L5 in Figure 1. In this report we provide an analytic solution for a general 3-D antenna and baseline placement with an arbitrary number of antennas. Such an analytic solution can be used for our upcoming 4-antenna BIMAP-3D arrays or any other interferometer arrays with three or more antennas.

We will further analyze the interferometric uncertainties related to the proposed generic processing technique. For a mapped lightning source location, it is important to understand the related uncertainty/error range and the associated confidence level, like in any other experimental and observational researches. However, only very limited and preliminary studies have been reported on the interferometric uncertainties in the lightning community (e.g., Stock et al., 2014, Shao et al., 2020). Without a credible estimate of the uncertainty, it is often possible to misinterpret the observations and to arrive to ambiguous and even erroneous conclusions. In this paper we present an analytic analysis based on the uncertainty propagation principles, from the time-delay uncertainty to the source error ellipses, and verify our analytic analysis with numerical experiments. Such an analytic uncertainty analysis will help to lay the foundation

for the upcoming interferometric studies with our new BIMAP-3D systems and will be also applicable on others' interferometer observations in the lightning community.

1. General Formulas for Source Direction Cosines

In this section we present a set of formulas that relate the direction cosines of a source to a pair of baselines that are formed with arbitrary antenna placements. A common coordinate frame is used for both the antenna and baseline placement and the source direction cosines (e.g., an East-North-Up (ENU) coordinate) such that the source direction can be directly obtained for any pair of arbitrary baselines without further geometric transformation.

For two spatially separated antennas at \mathbf{P}_1 and \mathbf{P}_2 , a baseline can be expressed as $\mathbf{L} = \mathbf{P}_2 - \mathbf{P}_1 = (a, b, c)$ in general in a right-hand Cartesian coordinate frame (X, Y, Z). The direction cosines of the source can be expressed in the same frame as $\mathbf{S} = (\alpha, \beta, \gamma)$, where $\alpha^2 + \beta^2 + \gamma^2 = 1$. The time delay detected between the two antennas can be expressed as $\mathbf{S} \bullet \mathbf{L} = -v\tau$, where v is the signal propagation speed, the speed of light for RF signal, and τ is the time delay measured from \mathbf{P}_2 to \mathbf{P}_1 of the baseline, or more explicitly

$$a\alpha + b\beta + c\gamma = -v\tau.$$

The source direction cosines can be determined with two different baselines \mathbf{L}_1 , \mathbf{L}_2 ,

$$\begin{aligned} a_1\alpha + b_1\beta + c_1\gamma &= -v\tau_1 \\ a_2\alpha + b_2\beta + c_2\gamma &= -v\tau_2 \end{aligned}$$

together with the relation of $\alpha^2 + \beta^2 + \gamma^2 = 1$, where \mathbf{L}_1 , \mathbf{L}_2 don't need to share a common antenna in an array composed of more than three antennas (e.g., L0 and L5 in Figure 1).

Through direct but somewhat laborious and lengthy algebraic derivations, one can arrive to the following analytic solutions for (α, β, γ) as functions of the baseline vectors and the corresponding time delay measurements

$$\begin{aligned} \alpha &= \frac{v[(a_2\tau_1 + a_1\tau_2)(\mathbf{L}_1 \bullet \mathbf{L}_2) - a_1\tau_1 L_2^2 - a_2\tau_2 L_1^2] \pm (b_2c_1 - b_1c_2)A_0}{|\mathbf{L}_1 \times \mathbf{L}_2|^2} \\ \beta &= \frac{v[(b_2\tau_1 + b_1\tau_2)(\mathbf{L}_1 \bullet \mathbf{L}_2) - b_1\tau_1 L_2^2 - b_2\tau_2 L_1^2] \pm (c_2a_1 - c_1a_2)A_0}{|\mathbf{L}_1 \times \mathbf{L}_2|^2} \\ \gamma &= \frac{v[(c_2\tau_1 + c_1\tau_2)(\mathbf{L}_1 \bullet \mathbf{L}_2) - c_1\tau_1 L_2^2 - c_2\tau_2 L_1^2] \pm (a_2b_1 - a_1b_2)A_0}{|\mathbf{L}_1 \times \mathbf{L}_2|^2} \end{aligned}$$

where,

$$A_0 = \sqrt{|\mathbf{L}_1 \times \mathbf{L}_2|^2 - v^2(\tau_1\mathbf{L}_2 - \tau_2\mathbf{L}_1)^2}$$

There exist two sets of possible solutions for (α, β) in the above equations due to the quadratic nature of the source direction cosines. In practice with all the antennas situated on the ground, the physically meaningful set of solutions can be obtained by selecting the set with the greater α value between the two solutions.

It is clear from the above equations that the two baselines \mathbf{L}_1 and \mathbf{L}_2 have to be in two different directions to provide a solution, or otherwise $|\mathbf{L}_1 \times \mathbf{L}_2|^2 = 0$. It is also clear that $|\mathbf{L}_1 \times \mathbf{L}_2|^2 - v^2(\tau_1 \mathbf{L}_2 - \tau_2 \mathbf{L}_1)^2$ need to be greater or equal to 0, which leads to

$$\frac{v^2 \tau_1^2}{L_1^2} + \frac{v^2 \tau_2^2}{L_2^2} - 2 \frac{v \tau_1}{L_1} \frac{v \tau_2}{L_2} \cos \varphi - \sin^2 \varphi \leq 0,$$

where φ is the angle between the two baseline vectors. This constraint can be used to evaluate if the two baselines detect a physically variable signal or if the data are dominated by uncorrelated noises.

Equation (3) can be directly applied on other idealized or simplified antenna and baseline placements. For a 2-dimensional flat array with all the antennas situated in the XY plane, the general form of Equation (3) can be simplified. For instance, if \mathbf{L}_1 and \mathbf{L}_2 are orthogonal to each other and are in the X and Y directions, $\mathbf{L}_1 = (a_1, 0, 0)$ and $\mathbf{L}_2 = (0, b_2, 0)$, Equation (3) can be simplified to

$$= -\frac{v \tau_1}{a_1} \quad = -\frac{v \tau_2}{b_2} \quad = \sqrt{1 - \left(\frac{v \tau_1}{a_1}\right)^2 - \left(\frac{v \tau_2}{b_2}\right)^2}$$

Equation (5) is familiar to the lightning researchers who place their three antennas in a horizontal, right-angle configuration.

In the case of a flat array that the two baselines are not orthogonal to each other, without losing the generality we can assume $\mathbf{L}_1 = (a_1, 0, 0)$, $\mathbf{L}_2 = (a_2, b_2, 0)$, and we have $\mathbf{L}_1 \bullet \mathbf{L}_2 = a_1 a_2$ and $|\mathbf{L}_1 \times \mathbf{L}_2| = a_1 b_2$, Equation (3) becomes

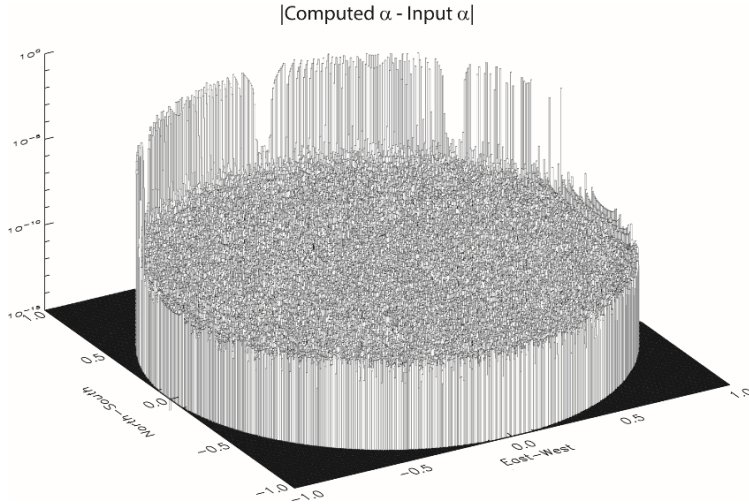
$$= -\frac{v \tau_1}{a_1}, \quad = -\frac{v \tau_2}{b_2} + \frac{v \tau_1 a_2}{a_1 b_2}, \quad = \sqrt{1 - \left(\frac{v \tau_1}{a_1}\right)^2 - \left(\frac{v \tau_2}{b_2}\right)^2 + \frac{v \tau_1 a_2 (2v \tau_2 a_1 - v \tau_1 a_2)}{(a_1 b_2)^2}}$$

Since α can be determined with known (β, γ) , in the following analysis we will only focus on (β, γ) .

With known α and β , the source direction in the azimuth and elevation (θ, ϕ) space can be simply obtained with

$$\phi = \text{atan} \frac{\beta}{\alpha}$$

$$\theta = \text{acos} \sqrt{\alpha^2 + \beta^2}$$



To verify the analytic solution in Equation (3), we excised a numerical experiment based on the array configuration shown in Figure 1. We divide the direction cosines of (α, β) into 400 X 400 grid points with a grid size of (0.005 X 0.005). For each grid point, which is corresponding to a certain source direction, we compute the time delays for each of the six baselines $(l, l=0,1, \dots 5)$ with Equation (1). We then select a pair of baselines with their corresponding time delays and compute backward the direction cosines (α, β) with Equation (3). For the two possible sets of solutions in Equation (3) we select the set that corresponding to the greater α value among its two possible values since the source is assumed to arrive from above the ground. It is noted here that both of the α values could be greater than zero since the baselines are assumed tilted from the true horizontal plane. We found that correct (α, β) are retrieved for all the possible pairs of baselines across the entire (α, β) space, verified that Equation (3) provides the correct and general analytic solutions.

Figure 2 demonstrates the test result for one of the baseline pairs (L0, L5 in Figure 1 which do not share a common antenna). The plot shows the difference between the retrieved and the input direction cosine α over the entire direction cosine space (-1 to +1 for α and β). In an ideal case, the difference would be zero across the entire (α, β) space. The residual differences of about 10^{-10} over the majority of the grid points are due to the finite grid resolution and the numerical resolution, and they are much finer than the resolution of a realistic interferometric measurement. The significant differences along the northern edge are due to the fact that L0 is tilted upward toward the north (Figure 1). At these grid points, the input source directions are actually below the L0 baseline (ground surface) that are unrealistic and would not be observed with an actual interferometer. Results for β and α show the same behavior as for α , and are not shown here.

1. Uncertainty Analysis

It is important to understand the uncertainty range and confidence level associated with the detected source direction based on the general interferometric processing proposed here, as in any experimental and observational researches. In this section we present the analytical uncertainty analysis and then verify the analytical results with numerical experiments.

3.1 Uncertainty for one pair of baselines

We start the uncertainty analysis with a single pair of baseline measurement, and extend the analysis to a combination of any number of baseline pairs in the next section. Assuming the systematic errors related to the antenna positions and the signal propagation through cables and electronics can be accurately calibrated, and assuming signals from all antennas are digitized and recoded with a phase-synchronized data acquisition system, the remaining random errors in (α, β) can be attributed to the errors in the time delay detection (τ_1, τ_2) between the antennas for each baseline.

To evaluate the variance and covariance for α and β , which defines the error/uncertainty ellipse, we need to carry out their partial derivatives respect to τ_1 and τ_2 due to the nonlinear dependence of α and β on τ_1 and τ_2 (e.g. Equation 3), under small error assumptions. From Equation (3) we have, for α ,

$$\begin{aligned}\frac{\partial \alpha}{\partial \tau_1} &= v \frac{[a_2(\mathbf{L}_1 \bullet \mathbf{L}_2) - a_1 L_2^2] \pm (b_2 c_1 - b_1 c_2) B_1}{|\mathbf{L}_1 \times \mathbf{L}_2|^2} \\ \frac{\partial \alpha}{\partial \tau_2} &= v \frac{[a_1(\mathbf{L}_1 \bullet \mathbf{L}_2) - a_2 L_1^2] \pm (b_2 c_1 - b_1 c_2) B_2}{|\mathbf{L}_1 \times \mathbf{L}_2|^2}\end{aligned}$$

Similarly for β we have

$$\begin{aligned}\frac{\partial \beta}{\partial \tau_1} &= v \frac{[b_2(\mathbf{L}_1 \bullet \mathbf{L}_2) - b_1 L_2^2] \pm (c_2 a_1 - c_1 a_2) B_1}{|\mathbf{L}_1 \times \mathbf{L}_2|^2} \\ \frac{\partial \beta}{\partial \tau_2} &= v \frac{[b_1(\mathbf{L}_1 \bullet \mathbf{L}_2) - b_2 L_1^2] \pm (c_2 a_1 - c_1 a_2) B_2}{|\mathbf{L}_1 \times \mathbf{L}_2|^2}\end{aligned}$$

where,

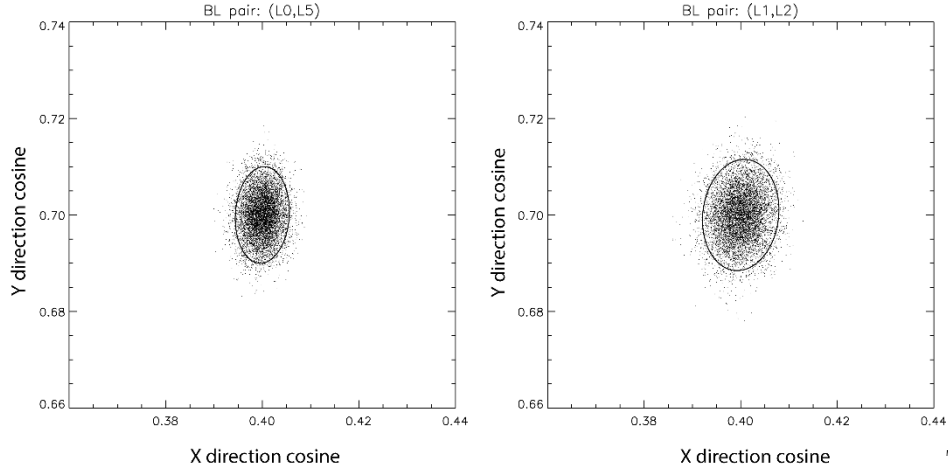
$$\begin{aligned}B_1 &= \frac{v[\tau_1 L_2^2 - \tau_2(\mathbf{L}_1 \bullet \mathbf{L}_2)]}{A_0} \\ B_2 &= \frac{v[\tau_2 L_1^2 - \tau_1(\mathbf{L}_1 \bullet \mathbf{L}_2)]}{A_0}\end{aligned}$$

It should be noted here that in Equations (8-9) the \pm signs correspond to the \pm signs in Equation (3). Once the correct set of solution for (α, β) is selected based on (τ_1, τ_2) , the same sign is used in Equations (8-9) in the uncertainty analysis.

Assuming τ_1 and τ_2 are independent with each other, the variance and covariance for α and β are expressed as, based on general error propagation principles (e.g., Arras, 1998)

$$\begin{aligned}\sigma_\alpha^2 &= \left(\frac{\partial\alpha}{\partial\tau_1}\right)^2 \sigma_{\tau_1}^2 + \left(\frac{\partial\alpha}{\partial\tau_2}\right)^2 \sigma_{\tau_2}^2 \\ \sigma_\beta^2 &= \left(\frac{\partial\beta}{\partial\tau_1}\right)^2 \sigma_{\tau_1}^2 + \left(\frac{\partial\beta}{\partial\tau_2}\right)^2 \sigma_{\tau_2}^2 \\ \sigma &= \sigma = \left(\frac{\partial\alpha}{\partial\tau_1} \frac{\partial\beta}{\partial\tau_1}\right) \sigma_{\tau_1}^2 + \left(\frac{\partial\alpha}{\partial\tau_2} \frac{\partial\beta}{\partial\tau_2}\right) \sigma_{\tau_2}^2\end{aligned}$$

Equation (10) defines the error ellipse in the (α, β) space, which is dependent on the geometry of the pair of the baselines, the source direction, and the error of time delays measured by the two baselines.



To verify the analytic error analysis (Equation 10), we compare its predictions with a numerical excise. Figure 3 illustrates the comparison for two selected baseline pairs, (L0, L5) and (L1, L2) in Figure 1. In the comparison, we chose a source direction of $(0.4, 0.7)$ in the (α, β) space and assumed σ_{τ_1} to be the same of 0.4 ns for all the baseline measurements. In general σ_{τ_1} are different for different baselines and are dependent on the direction of the source. However, if one apply the beam-steering interferometry technique introduced in Shao et al. (2020), σ_{τ_1} approach approximately the same for all the baselines. As also discussed in Shao et al. (2020), the time delay error σ_{τ_1} can be estimated based on the signal-to-noise ratio, the interferometer's RF bandwidth, and the time widow used for the signal correlation computation. In the current study, we assumed σ_{τ_1} are known and the readers are referred to Shao et al. (2020) for the analysis of σ_{τ_1} .

In this excise, the actual time delay for the source at $(0.4, 0.7)$ for each baseline is computed with Equation (1). In the numerical calculation, the actual time delay for each baseline is added with an independent and random time error that has a standard deviation of σ_{τ_1} , and the corresponding direction cosines are then computed by using Equation (3) for the selected baseline pairs. The scattered dots in each plot in Figure 3 show the results for such a numerical excise with 10^4 iterations. The overlapped error ellipse in each plot is computed analytically from Equation (10). In the plot, we chose a confidence level of 90% for the size

of error ellipse, meaning that there is a 90% of probability that the true result will fall within the ellipse. For a 68% confidence level, the one-sigma level, the size of the ellipse would be scaled down by a factor of 2.1. It is clear from Figure 3 that the analytic error prediction is in agreement with the numerical experiment.

We now further derive the corresponding variance and covariance in the azimuth and elevation angle (α, θ) space. For a general pair of baselines, α and θ cannot be assumed independent, as indicated by the covariance term in Equation (10) and as shown in Figure 3, unless the two baselines are orthogonal to each other (e.g., Equation 5). Therefore, we have, based on the error propagation principles,

$$\begin{aligned}\sigma_\phi^2 &= \left(\frac{\partial\phi}{\partial\alpha}\right)^2 \sigma_\alpha^2 + \left(\frac{\partial\phi}{\partial\beta}\right)^2 \sigma_\beta^2 + 2\left(\frac{\partial\phi}{\partial\alpha}\frac{\partial\phi}{\partial\beta}\right) \sigma \\ \sigma_\theta^2 &= \left(\frac{\partial\theta}{\partial\alpha}\right)^2 \sigma_\alpha^2 + \left(\frac{\partial\theta}{\partial\beta}\right)^2 \sigma_\beta^2 + 2\left(\frac{\partial\theta}{\partial\alpha}\frac{\partial\theta}{\partial\beta}\right) \sigma \\ \sigma &= \left(\frac{\partial\phi}{\partial\alpha}\frac{\partial\theta}{\partial\alpha}\right) \sigma_\alpha^2 + \left(\frac{\partial\phi}{\partial\beta}\frac{\partial\theta}{\partial\beta}\right) \sigma_\beta^2 + \left(\frac{\partial\phi}{\partial\alpha}\frac{\partial\theta}{\partial\beta} + \frac{\partial\phi}{\partial\beta}\frac{\partial\theta}{\partial\alpha}\right) \sigma\end{aligned}$$

Using $\alpha = \cos\theta \cos\phi$ and $\beta = \cos\theta \sin\phi$ we have

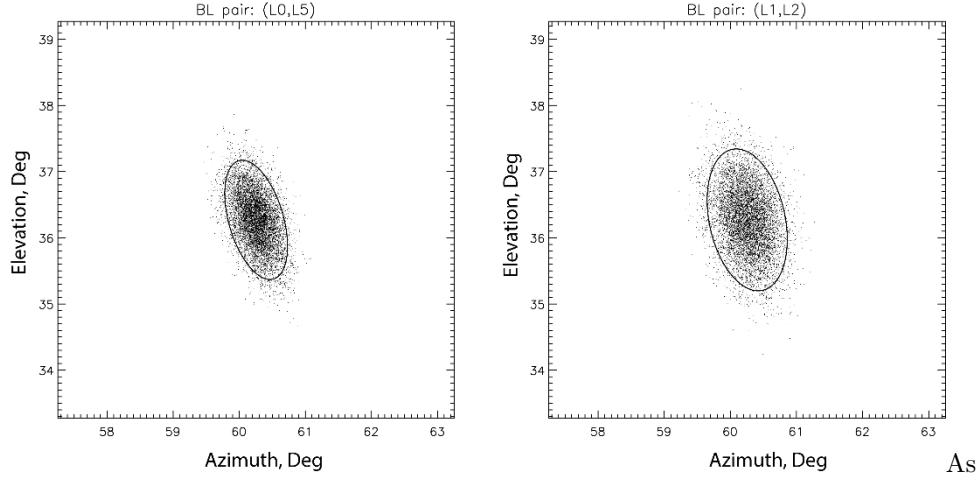
$$\begin{aligned}\frac{\partial\phi}{\partial\alpha} &= -\frac{\sin\phi}{\cos\theta}, & \frac{\partial\phi}{\partial\beta} &= +\frac{\cos\phi}{\cos\theta}, \\ \frac{\partial\theta}{\partial\alpha} &= -\frac{\cos\phi}{\sin\theta}, & \frac{\partial\theta}{\partial\beta} &= -\frac{\sin\phi}{\sin\theta}\end{aligned}$$

Equation (11) becomes

$$\begin{aligned}\sigma_\phi^2 &= \frac{1}{\cos^2\theta} \left(\sin^2\phi \sigma_\alpha^2 + \cos^2\phi \sigma_\beta^2 - \sin 2\phi \sigma \right) \\ \sigma_\theta^2 &= \frac{1}{\sin^2\theta} \left(\cos^2\phi \sigma_\alpha^2 + \sin^2\phi \sigma_\beta^2 + \sin 2\phi \sigma \right) \\ \sigma &= \frac{1}{\sin 2\theta} \left[\sin 2\phi \left(\sigma_\alpha^2 - \sigma_\beta^2 \right) - 2 \cos 2\phi \sigma \right]\end{aligned}$$

where σ_α and σ_β can be computed with Equation (7) from (α, θ) .

Similar to Figure 3, Figure 4 shows the corresponding comparisons for the error analyses in the (α, θ) space. The scattered dots are converted directly from (ϕ, θ) to (α, θ) with Equation (7), and the corresponding analytic ellipses are computed analytically based on Equation (13). As expected, good agreements are observed.



noted earlier, interferometric errors depend on the baseline geometries, the source direction, and the error of the time delay measurement over the baselines. It is clear in Figures 3 and 4 that for the same source direction and the same time error, the error ellipses are clearly different for the two different pairs of baselines. Although not shown here, it is also evident that for a source in a different direction, the error ellipses will also be different. This is part of the reason why it is important to be able to compute the error level analytically. With this, one can directly and straightforwardly estimate the level of the direction errors for sources from any directions with any antenna and baseline configurations.

3.2 Combination of multiple pairs of baselines

To estimate the source direction cosines (,) from multiple pairs of baselines, the most straightforward approach is to compute the arithmetic average of and among all the baseline pair measurements, especially when there is no pre-knowledge of the source direction in a normal interferometric process. Assuming the number of independent baselines is N (6 in Figure 1), the arithmetic mean can be expressed as functions of $\tau_l : l = 1, 2, \dots, N$, i.e.,

$$\begin{aligned} \bar{\alpha} &= \frac{2}{N(N-1)} \sum_{l=1}^{N-1} \sum_{m=l+1}^N \alpha(\tau_l, \tau_m) \\ \bar{\beta} &= \frac{2}{N(N-1)} \sum_{l=1}^{N-1} \sum_{m=l+1}^N \beta(\tau_l, \tau_m) \end{aligned}$$

The variance for – can be computed in general by, again based on error propagation principles

$$\sigma_{\bar{\alpha}}^2 = \sum_{i=1}^N \left(\frac{\partial \bar{\alpha}}{\partial \tau_i} \right)^2 \sigma_{\tau_i}^2 + \sum_i^N \sum_{j \neq i}^N \left(\frac{\partial \bar{\alpha}}{\partial \tau_i} \right) \left(\frac{\partial \bar{\alpha}}{\partial \tau_j} \right) \sigma_{\tau_i \tau_j}$$

Because the uncertainties for the time delays for different baselines can be as-

sumed independent, the 2nd term in the above equation can be assumed to be zero. We then have, by using Equations (14) and (15),

$$\sigma_{\bar{\alpha}}^2 = \left[\frac{2}{N(N-1)} \right]^2 \sum_{i=1}^N \left[\sum_{l=1}^{N-1} \sum_{m=l+1}^N \frac{\partial \alpha(\tau_l, \tau_m)}{\partial \tau_i} \right]^2 \sigma_{\tau_i}^2$$

Similarly for $\bar{\beta}$ we have

$$\sigma_{\bar{\beta}}^2 = \left[\frac{2}{N(N-1)} \right]^2 \sum_{i=1}^N \left[\sum_{l=1}^{N-1} \sum_{m=l+1}^N \frac{\partial \beta(\tau_l, \tau_m)}{\partial \tau_i} \right]^2 \sigma_{\tau_i}^2$$

For the covariance between $\bar{\alpha}$ and $\bar{\beta}$ we have

$$\sigma_{\bar{\alpha}\bar{\beta}} = \left[\frac{2}{N(N-1)} \right]^2 \sum_{i=1}^N \left\{ \left[\sum_{l=1}^{N-1} \sum_{m=l+1}^N \frac{\partial \alpha(\tau_l, \tau_m)}{\partial \tau_i} \right] \left[\sum_{l=1}^{N-1} \sum_{m=l+1}^N \frac{\partial \beta(\tau_l, \tau_m)}{\partial \tau_i} \right] \right\} \sigma_{\tau_i}^2$$

The differentials in Equations (16-18) can be computed from Equations (8-9).

For example, for a three-baseline interferometer that has been used presently by many research institutes the uncertainties can be estimated with the following explicit formulas

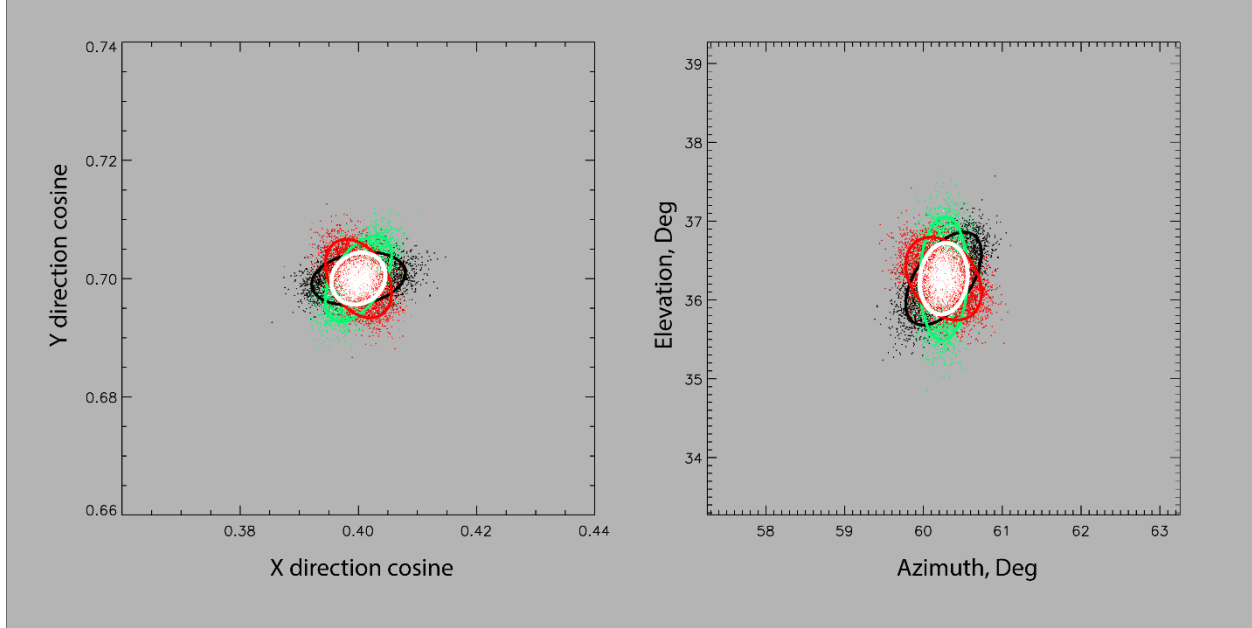
$$\begin{aligned} \sigma_{\bar{\alpha}}^2 &= \frac{1}{9} \left\{ \left[\frac{\partial a_{12}}{\partial \tau_1} + \frac{\partial a_{13}}{\partial \tau_1} \right]^2 \sigma_1^2 + \left[\frac{\partial a_{12}}{\partial \tau_2} + \frac{\partial a_{23}}{\partial \tau_2} \right]^2 \sigma_2^2 + \left[\frac{\partial a_{13}}{\partial \tau_3} + \frac{\partial a_{23}}{\partial \tau_3} \right]^2 \sigma_3^2 \right\} \\ \sigma_{\bar{\beta}}^2 &= \frac{1}{9} \left\{ \left[\frac{\partial \beta_{12}}{\partial \tau_1} + \frac{\partial \beta_{13}}{\partial \tau_1} \right]^2 \sigma_1^2 + \left[\frac{\partial \beta_{12}}{\partial \tau_2} + \frac{\partial \beta_{23}}{\partial \tau_2} \right]^2 \sigma_2^2 + \left[\frac{\partial \beta_{13}}{\partial \tau_3} + \frac{\partial \beta_{23}}{\partial \tau_3} \right]^2 \sigma_3^2 \right\} \\ \sigma_{\bar{\alpha}\bar{\beta}} &= \frac{1}{9} \left\{ \left[\frac{\partial a_{12}}{\partial \tau_1} + \frac{\partial a_{13}}{\partial \tau_1} \right] \left[\frac{\partial \beta_{12}}{\partial \tau_1} + \frac{\partial \beta_{13}}{\partial \tau_1} \right] \sigma_1^2 + \left[\frac{\partial a_{12}}{\partial \tau_2} + \frac{\partial a_{23}}{\partial \tau_2} \right] \left[\frac{\partial \beta_{12}}{\partial \tau_2} + \frac{\partial \beta_{23}}{\partial \tau_2} \right] \sigma_2^2 + \left[\frac{\partial a_{13}}{\partial \tau_3} + \frac{\partial a_{23}}{\partial \tau_3} \right] \left[\frac{\partial \beta_{13}}{\partial \tau_3} + \frac{\partial \beta_{23}}{\partial \tau_3} \right] \sigma_3^2 \right\} \end{aligned}$$

where, α_{12} stands for $\alpha(\tau_1, \tau_2)$ for baselines 1 and 2, and so forth.

To find the variance and covariance in the azimuth and elevation ($\bar{\phi}, \bar{\theta}$) space, we can simply substitute ($\sigma_{\bar{\alpha}}^2, \sigma_{\bar{\beta}}^2, \sigma_{\bar{\alpha}\bar{\beta}}$) in to Equation (13), with the corresponding ($\bar{\phi}, \bar{\theta}$) computed with Equation (7).

Figure 5 illustrates the combination results for three pairs of baseline measurements, based on the three longest baselines L3, L4, and L5 in Figure 1. Similar to Figures 3 and 4, the black, green, and red dots and their corresponding ellipses are for each individual baseline pairs of (L3, L4), (L3, L5), and (L4, L5), respectively. The white dots are the arithmetic average of the three colored dots at each of the 10^4 iterations, computed with Equation (14). The white ellipse is computed based on the variance and covariance Equations (16-18), or explicitly Equation (19) in this three-pair case. It is clear that the analytic error analysis

for the combined baseline pairs (the white ellipse) agrees with the numerical experiment (white dots). As in Figures 3 and 4, the ellipses indicate the 90% confidence level.

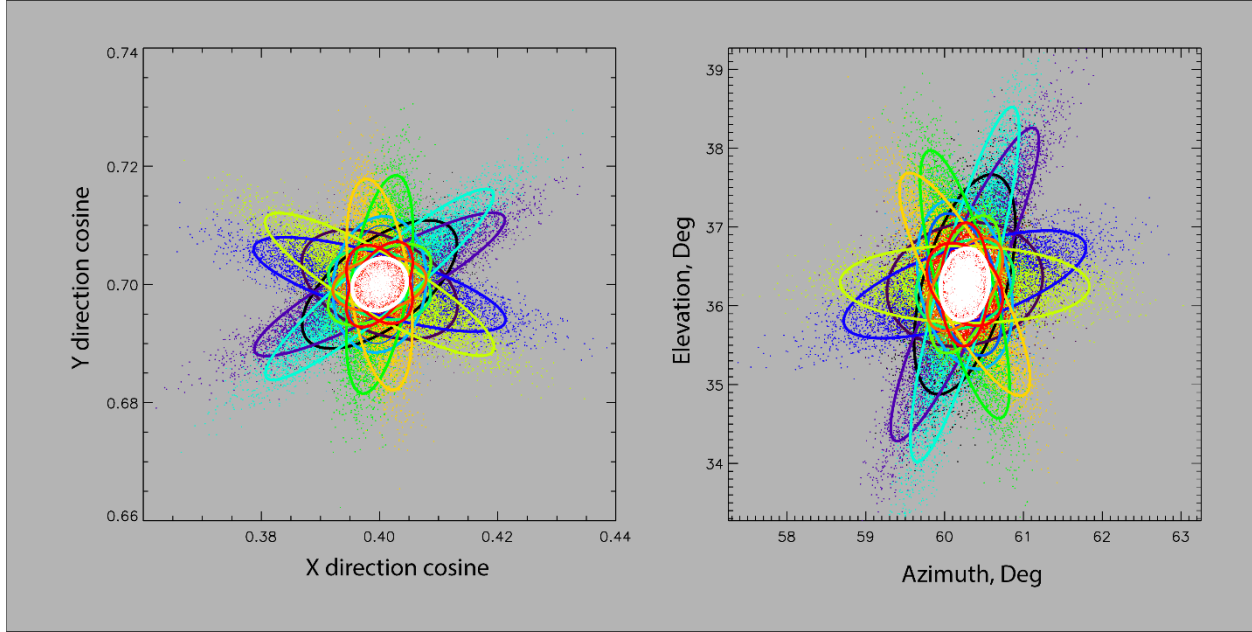


should be noted here that since the three pairs of baselines are correlated with each other, as shown in Equations (16-18), the combined error do not have a factor of 3 reduction as would be expected for totally independent measurements. Instead, the combined error ellipse (white) is inscribed within the three individual error ellipses (colored).

Finally we present the results for all the possible pairs of baselines. For a 4-antenna array (e.g., Figure 1) we have 6 independent baselines ($\binom{4+3}{2}$). With 6 baselines, we have 15 ($\binom{6+5}{2}$) unique combinations of pair of baselines. Figure 6 shows the error ellipses for all the individual pairs (colored) and the error ellipse (white) after the arithmetic average of all the pairs. The combined error ellipse is computed with Equations (16-18). Similar to that in Figure 5, the combined error ellipse is inscribed by the smallest three individual ellipses, in this case the same three individual ellipses shown in Figure 5. These smallest individual ellipses correspond to the three pairs of the longest baselines in the array (L3, L4, L5, in Figure 1). Therefore, Figures 6 and 5 show that the size of the error ellipse after the arithmetic average is determined by the longest baselines in the array. In other words, the finest interferometric resolution for the array is determined by the longest baselines.

The question is then how do the other redundant, shorter baselines help the overall interferometric process? In practice, signals detected by a longer baseline will have a greater time delay between their two corresponding antennas, and the

signals are less correlated in a normal interferometric process, such that the time delay estimate could be less accurate or sometimes erroneous, and the resultant source direction could be ambiguous. In the opposite, the signals over the shorter baselines are more correlated and the measurement is less likely to provide a wrong source direction. The combination of all the baseline measurements then intend to provide a correct measurement for the source direction.



once the correct but coarse source direction is determined, one can apply the beam-steering interferometry technique introduced in Shao et al. (2020) to further improve the mapping resolution. The beam-steering interferometry shifts the signals among all the antennas to align the signals in time based on the source direction estimated in a first-stage normal interferometric process. As such, signals among all the antennas have the maximum correlation over all the baseline measurements, and the errors of time delay for all the baselines intend to be the same and to be minimized. In this case, simply using the longest baselines in the array will provides the same accurate results as that using the combination of all the baselines. It is also possible to map multiple sources at each chosen time window with an iterative process by applying the beam-steering interferometry. But this is beyond the scope of this paper and will be investigated in future studies.

1. Summary

In this paper, we present an analytic solution for a general 3-dimensional antenna and baseline placement for a broadband RF lightning interferometer. The analytic formulas directly relate the source direction in the direction cosine space (θ, ϕ) to the baseline vectors in the same coordinate frame, and to the signal

time delays measured over the baselines. The analytic solution is compared against a numerical experiment and is verified to be correct to within the simulation and numerical precision. Such a general solution can be used in existing 3-antenna arrays, and more importantly in arrays with more than three antennas that are less likely situated in the same plane.

We also present analytic error/uncertainty analyses for a pair of baseline measurement and for a combination of multiple pairs of baselines, based on error propagation principles. The error analysis is presented in both the direction cosine space and the azimuth-elevation space. The analytic error solutions are also verified with a set of numerical experiments. Error estimate is important in the rapidly developing and increasingly widely used broadband lightning interferometry for credible and unambiguous interpretation of the observed results. The analytic formulas in this paper will help to lay the foundation for future error analysis in the interferometric lightning studies.

We should note that the combined error analysis presented here is based on the arithmetic average of the multiple pairs of baseline measurements. This is especially applicable on a normal interferometric process during which the source direction is unknown. If one applies a 2nd-stage beam-steering interferometry after the normal interferometry with the known source direction, one can obtain the variance and covariance for the specific source direction and an error-weighted average among the baseline pairs can be used. The corresponding error range with the weighted average is expected to be reduced. However, the analytic error analysis becomes more complicated and will be investigated in a future study.

Acknowledgments

This work was supported by the Los Alamos National Laboratory’s Pathfinder Project WC3N 21EMP0L and by the National Nuclear Security Administration of the U.S. Department of Energy’s project H7HE PAARMEO0.

References:

- Arras, K. O. (1998). An Introduction to Error Propagation: Derivation, Meaning and Examples of Equation $C_y = F_X C_X F_X^T$, Technical Report, No: EPFL-ASL-TR-98-01 R3, the Autonomous Systems Lab, Institute of Robotic Systems, Swiss Federal Institute of Technology Lausanne.
- Belz, J. W. e. a. (2020). Observations of the origin of downward terrestrial gamma-ray ashes. *Journal of Geophysical Research: Atmospheres*, 125 (23), e2019JD031940.
- Dong, W., X. Liu, Y. Y., & Zhang, Y. (2001). Broadband interferometer observations of a triggered lightning. *Chinese Science Bulletin*, 46(18), 1561– 1565.
- Huang, A., S. A. Cummer, Y. Pu, Lightning Initiation From Fast Negative Breakdown is Led by Positive Polarity Dominated Streamers, *Geophysical Research Letters*, 10.1029/2020GL091553, 48, 8, (2021).

- Jensen, D. P., Sonnenfeld, R. G., Stanley, M. A., Edens, H. E., da Silva, C. L., Krehbiel, P. R. (2021). Dart-leader and k-leader velocity from initiation site to termination time-resolved with 3d interferometry. *Journal of Geophysical Research: Atmospheres*, (p. e2020JD034309).
- Lyu, F., S. A. Cummer, Z. Qin, M. Chen, Lightning Initiation Processes Imaged With Very High Frequency Broadband Interferometry, *Journal of Geophysical Research: Atmospheres*, 10.1029/2018JD029817, **124**, 6, (2994-3004), (2019).
- Rison, W., Krehbiel, P. R., Stock, M. G., Edens, H. E., Shao, X.-M., Thomas, R. J., Stanley, M. A., & Zhang, Y. (2016). Observations of narrow bipolar events reveal how lightning is initiated in thunderstorms. *Nature Communications*, 7, 10721.
- Shao, X. M., Holden, D. N., & Rhodes, C. T. (1996). Broad band radio interferometry for lightning observations. *Geophysical Research Letters*, 23(15), 1917–1920.
- Shao, X. M., & Jacobson, A. R. (2001). Polarization observations of broadband VHF signals by the FORTE satellite. *Radio Science*, 36(6), 1573– 1589.
- Shao, X.-M., & Jacobson, A. R. (2002). Polarization observations of lightning-produced VHF emissions by the FORTE satellite. *Journal of Geophysical Research*, 107(D20), 4430.
- Shao, X.-M., Ho, C., Caffrey, M., Graham, P., Haynes, B., Bowers, G., Blaine, W., Dingus, B., Smith, D., & Rassoul, H. (2018). Broadband RF interferometric mapping and polarization (BIMAP) observations of lightning discharges: Revealing new physics insights into breakdown processes. *Journal of Geophysical Research: Atmospheres*, 123, 10,326– 10,340.
- Shao, X.-M., Ho, C., Bowers, G., Blaine, W., & Dingus, B. (2020). Lightning interferometry uncertainty, beam steering interferometry, and evidence of lightning being ignited by a cosmic ray shower. *Journal of Geophysical Research: Atmospheres*, 125, e2019JD032273.
- Stock, M. G., Akita, M., Krehbiel, P. R., Rison, W., Edens, H. E., Kawasaki, Z., & Stanley, M. A. (2014). Continuous broadband digital interferometry of lightning using a generalized cross-correlation algorithm. *Journal of Geophysical Research: Atmospheres*, 119, 3134– 3165.
- Stock, M. G., Krehbiel, P. R., Lapierre, J., Wu, T., Stanley, M. A., & Edens, H. E. (2017). Fast positive breakdown in lightning. *Journal of Geophysical Research: Atmospheres*, 122, 8135– 8152.
- Sun, Z., Qie, X., Liu, M., Cao, D., & Wang, D. (2013). Lightning VHF radiation location system based on short-baseline TDOA technique—Validation in rocket-triggered lightning. *Atmospheric Research*, 58, 129– 130.
- Tilles, J. N., Liu, N., Stanley, M. A., Krehbiel, P. R., Rison, W., Stock, M. G., Dwyer, J. R., Brown, R., & Wilson, J. (2019). Fast negative breakdown in

thunderstorms. *Nature Communications*, 10, 1648.

Figure captions:

Figure 1. Antenna array for one of two BIMAP-3D interferometers. Note that the four antennas are not in a horizontal plane or a common plane. The heights are different in meters among the antennas.

Figure 2. Difference between retrieved and input direction cosine in the entire (α, δ) space. The baseline pair of L0 and L5 in Figure 1 are used for this plot. The majority of the points are in agreement within about 10^{-10} , showing correct source directions are retrieved. Points at the northern edge are due to the input directions beneath the L0 baseline which would not occur in real observations.

Figure 3. Analytic error ellipse compared with numerical test for two selected baseline pairs (L0, L5) and (L1, L2). The scattered dots shows the numerical results and the error ellipses are based on the analytic calculations. The error ellipses are plotted at the 90% confidence level.

Figure 4. Similar to Figure 3, but shows the error analyses in (α, δ) space.

Figure 5. Interferometric results and error estimate for a combination of three baseline (L3, L4 and L5 in Figure1) measurement. The colored dots and ellipses are for each individual baseline pairs, similar to that in Figure 3 and 4. The white dots are the arithmetic average of the colored dots, and the white ellipse is the error ellipse based on Equations (16-18). The left plot is for (α, δ) and the right plot is for (α, δ) .

Figure 6. Similar to Figure 5, but for all the possible 15 pairs of baselines for the 4-antenna array in Figure 1. The left plot is for (α, δ) and the right plot is for the corresponding (α, δ) .